ACS MATERIALS Au
AN OPEN ACCESS JOURNAL OF THE AMERICAN CHEMICAL SOCIETY

pubs.acs.org/materialsau

Article

Joule Heating-Driven Transformation of Hard-Carbons to Onion-like Carbon Monoliths for Efficient Capture of Volatile Organic Compounds

Itisha Dwivedi and Chandramouli Subramaniam*

Cite This: ACS Mater. Au 2022, 2, 154–162

Read Online

ACCESS | Metrics & More | Article Recommendations | Supporting Information

ABSTRACT: Soft graphitizable carbon-based multifunctional nanomaterials have found versatile applications ranging from energy storage to quantum computing. In contrast, their hard-carbon analogues have been poorly investigated from both fundamental and application-oriented perspectives. The predominant challenges have been (a) the lack of approaches to fabricate porous hard-carbons and (b) their thermally nongraphitizable nature, leading to inaccessibility for several potential applications. In this direction, we present design principles for fabrication of porous hard-carbon-based nanostructured carbon florets (NCFs) with a highly accessible surface area (~936 m^2/g), rivalling their soft-carbon counterparts. Subjecting such thermally stable hard-carbons to a synergistic combination of an electric field and Joule heating drives their transformation to free-standing macroscopic monoliths composed of onion-like carbons (OLCMs). This represents the first such structural transformation observed in sp^2-based hard-carbon NCFs to sp^2-networked OLCMs. Micro-Raman spectroscopy establishes the simultaneous increase in the intensity of D-, 2D-, and D + G-bands at 1341, 2712, and 2936 cm^{-1} and is correlated to the reorganization in the disordered graphitic domains of NCFs to curved concentric nested spheres in OLCMs. This therefore completely precludes the formation of a nanodiamond core that has been consistently observed in all previously reported OLCs. The Joule heating-driven formation of OLCMs is accompanied by ~5700% enhancement in electrical conductivity that is brought about by the fusion of outermost graphitic shells of OLCs to result in monolithic OLC structures (OLCMs). The porous and inter-networked OLCMs exhibit an excellent adsorption-based capture of volatile organic compounds such as toluene at high efficiencies (~99%) over a concentration range (0.22–1.86 ppm) that is relevant for direct applications such as smoke filters in cigarettes.

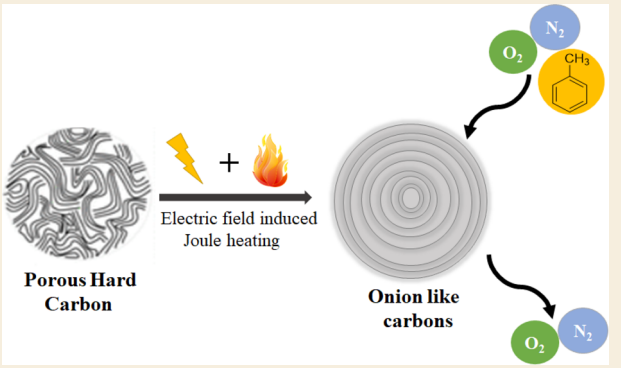

KEYWORDS: *hard-carbons, Joule heating, onion-like carbons, VOC capture, adsorption*

INTRODUCTION

Carbon along with its allotropic variations represents a vital bridge between the natural and artificial worlds.[1−3] Discovery of new allotropes has been continuously receiving attention over the past four decades and has seen the emergence of exciting scientific phenomena, leading to a wide range of applications.[4−15] Simultaneous interest in approaches and pathways for interconversion between such allotropes leading to multifunctional materials is gathering increased significance.[16−19] Such interconversions are endothermic and extremely slow processes, such as the natural conversion of graphite to diamond. Therefore, the desire to enhance and control the kinetics of such allotropic interconversions demands unconventional approaches compared to those adopted for C−H activation and C═C bond formation.[20,21] Accordingly, various forms of energy such as high-pressure, laser-ablation, photothermal, and electric and thermal fields have been utilized to drive these transformations in the desired directions.[1−3,10,22,23]

One of the earliest transformations involved thermal annealing of nanodiamonds at temperatures reaching up to 2000 °C under inert/vacuum conditions, leading to formation of onion-like carbons (OLCs). Subsequently, such sp^3 to sp^2 transformations were also demonstrated through electron beam irradiation on carbon black to form carbon nanotubes (CNTs) and OLCs. The formation of concentrically nested rings from nanodiamonds[24−26] received significant interest

Received: October 15, 2021
Revised: November 15, 2021
Accepted: November 19, 2021
Published: November 30, 2021

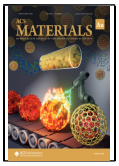

https://doi.org/10.1021/acsmaterialsau.1c00062
ACS Mater. Au 2022, 2, 154–162

from both a mechanistic standpoint[27] and for their applications in high power supercapacitors[28,29] and solid lubricants.[30] Therefore, while this approach produces a high yield of OLCs, its energy-intensive nature and a range of byproducts obtained owing to lack of control over the conversions have been its major drawback. In comparison, the production of OLCs through arc discharge[31,32] yields highly crystalline materials but at low yields, thereby demanding exhaustive purification protocols. While thermal annealing proceeds under kinetically controlled conditions, it results in formation of other byproducts such as carbon nanohorns and nanotubes and thereby requires detailed purification and separation protocols.

Accordingly, absolute structural uniformity with high yield over the end product (OLCs) is desirable. Further, the large scope for direct applications of OLCs has been severely limited due to the familiar problem of quantum effects degrading in macroscopic ensembles and at macroscopic dimensions.[33] Significantly, the predominant focus has been on the interconvertibility between the soft-carbons that exhibit propensity for both catenation and graphitization. Accordingly, these routes proceed through metastable intermediates but always tend toward the thermodynamically preferred crystalline end products.

In comparison, hard-carbons are structurally and thermally rigid and therefore are not envisaged for such interconversions. Hard-carbons consist of randomly oriented graphitic domains with an expanded d-spacing (~0.4 nm).[34] The existence of short-range graphitic ordering and long-range disordered domains is entropically unsuitable for catenative cross-linking, as supported by the lack of any investigations in this direction. A significant bottleneck lies in the lack of rational design approaches to fabricate such high entropic hard-carbons.[35−40] Conventional approaches involving pyrolysis of thermosetting polymers result in complete pore collapse and therefore yield bulk-phase hard-carbons with insignificant porosity and surface areas. Therefore, nanostructuring pathways for fabricating hard-carbons, analogous to those available for soft-carbons, are desirable yet lacking. The dimensional long-range disorder in hard-carbons and the resulting entropic penalty offer a distinct possibility to capture and stabilize OLCs. Therefore, the opportunity to create functional nanostructures of higher order and simultaneously understand the feasibility of such transformations in hard-carbons motivated the current investigation.

In this direction, we present two results in this work: (a) a rational approach based on robust design principles to fabricate hard-carbon nanostructures with well-defined porosity and engineered morphology (i.e., nanocarbon florets, NCFs) that enables (b) formation of macroscale OLC monoliths (OLCMs) through a combination of electromigrative and thermomigrative driving forces. The OLCMs (5 mm in length and 1 mm in diameter) represent a macroscopic structure that is uniformly constructed with OLCs (6.5 ± 1.2 nm) as building blocks and fused through strong covalent C═C linkages. Thereby, the OLCM provides a pathway for synergistic emergence of nanoscale properties in macroscopic discrete solids as seen from characteristic optical phonons that dominate the material over macroscopic dimensions of the monolith. The endothermic conversion of NCFs to OLCMs is driven by an electric field (1.7×10^3 V/m) and the associated Joule heating-based thermal fields, generating temperatures of ~2200 °C. The precise and uniform conversion of NCFs to OLCMs is established through both microscopy and spectroscopic results that corroborate to the stepwise reorganization of the long-range disordered domains into spherical Matryoshka-doll-like OLCs that further undergo cross-linking to form the OLCMs. The retention of porosity and the strained d-spacing (2.95 Å) over macroscopic dimensions in OLCMs has been utilized for direct capture of volatile organic compounds (VOCs) in a flow-through geometry over a wide concentration range (0.22 to 1.86 ppm) that is typically encountered in cigarette filters.

MATERIALS AND METHODS

Synthesis of NCFs

Dendritic fibrous nanosilica (DFNS) served as the template for fabrication of NCFs and was synthesized through a reported procedure.[41,42] The synthesis of nanocarbon florets was carried out by passing acetylene (carbon source, 100 sccm) over DFNS in an alumina boat under a He atmosphere (700 sccm) at 740 °C (10 °C/min ramp rate). After cooling, a black powdered sample was etched with 1 M NaOH for 5 h followed by repetitive washing with DI water till the pH of the supernatant became neutral. It was oven-dried at 80 °C to obtain nanocarbon florets (NCFs).

Synthesis of Monoliths

NCFs (5 mg) were loaded into a cylindrical quartz tube with a length of 5 cm and an inner diameter of 1 mm that is open at both ends. All experiments were conducted on the NCF packed over a length of 5 mm inside such a cylindrical quartz tube. Two copper electrodes inserted on either side provided electrical contacts to the NCF, while the quartz tube enabled thermometric imaging. The copper electrodes were held in place using shrink tubes after degassing the setup in a vacuum desiccator for 15 min. The electrical measurements were carried out by connecting the copper electrodes to a DC voltage supply (GW INSTEK GPS-3303) that allowed simultaneous monitoring of current. The OLCM was sliced with a knife blade for cross-sectional measurements.

Material Characterization

Ex situ electrical measurements on OLCMs were done using a Biologic VMP300 electrochemical workstation. Scanning electron microscopy was carried out at an accelerating voltage of 5 kV using a Carl-ZEISS Ultra 55 Field Emission Scanning Electron Microscope. Transmission electron microscopy was acquired with an FEI Tecnai G2, F30, at an accelerating voltage of 300 kV. The OLCM was crushed, dispersed in isopropyl alcohol, dropped onto carbon-coated copper TEM grids, and dried in an ambient atmosphere before imaging. Powder X-ray diffraction (XRD) patterns of samples were obtained using a powder X-ray diffractometer (Rigaku, Cu-Kα radiation, 1.514 Å) at a scan rate of 5 deg/min. Raman characterizations (spectra and imaging) were carried out using a WiTec micro-Raman spectrometer equipped with a Nd-YAG (532 nm) laser source. A 50× objective lens (N.A. 0.8) was used to focus the laser onto the sample. Raman imaging was carried out by collecting 10,000 spectra over the desired area to generate color-coded images. Confocal depth profiling was carried out over a depth of 200 μm that was divided into 13 layers. The layers were subsequently integrated using ImageJ to generate a three-dimensional volume map. All spectra were acquired within 30 s using a grating of 1200 grooves/mm and a laser power of 2 mW. No laser-induced change in the sample was observed under these conditions and confirmed through repeated spectra taken at the same location.

RESULTS AND DISCUSSION

Hard-carbons have been traditionally synthesized through high-temperature pyrolysis of thermosetting polymers.[34] Although scalable, this route suffers from the lack of any structural, chemical, and morphological control. Therefore, rational design approaches for hard-carbons, analogous to

https://doi.org/10.1021/acsmaterialsau.1c00062
ACS Mater. Au 2022, 2, 154−162

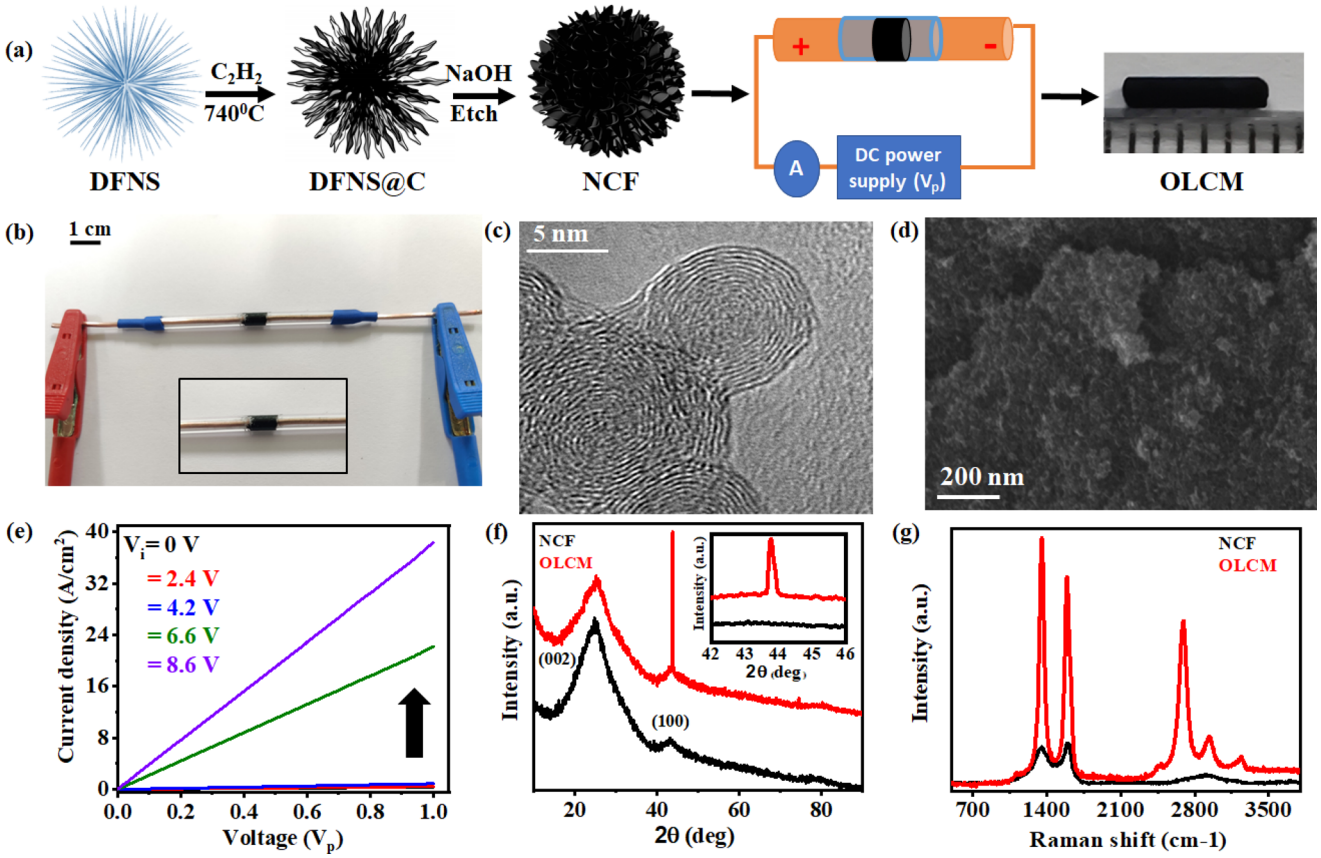

Figure 1. (a) Schematic representation of fabrication of the OLCM from the hard-carbon NCF, going through the steps of electric field-induced Joule heating. (b) Picture of the electrical setup containing the packed NCF in a quartz tube with Cu electrodes. The inset shows the magnified view of the NCF column. (c) HR-TEM of the OLCM. (d) SEM image of the OLCM showing fused structures. (e) Variation of current−voltage characteristics at various stages of conversion of the NCF to OLCM. (f) pXRD of the NCF and OLCM (inset: zoomed in graph showing a sharp peak at 43.8° for OLCM). (g) Raman spectra of the NCF and OLCM.

those present for their soft counterparts such as CNTs, graphene, and fullerenes, are lacking. Hard-carbons are a structurally high-entropic combination of graphitic stacking in the short range and highly disordered randomly oriented graphitic domains in the long range, thereby presenting distinct challenges in design principles. In order to overcome this, we based our approach in utilizing an amorphous thermally stable SiO_2 framework in the form of DFNS as the template (Figure 1a and Figure S1). As opposed to conventional polymer infiltration approaches that suffer from poor infiltration and inefficient templating,[43] we introduced the carbon precursors through gas-phase diffusion with DFNS as the substrate. The epitaxial deposition of carbon over the amorphous SiO_2 framework introduces the orientational randomness, while the kinetics of the chemical vapor deposition controlled the thickness of carbon coating (Figure 1a and Figure S1). The uniform deposition of the carbon and the subsequent complete removal of DFNS are confirmed from both SEM-EDS and TEM images (Figures S1 and S2) Accordingly, short-range stacking and long-range disorder, characteristics of hard-carbons, are obtained after removal of the DFNS template. The resulting complimentary carbon nanostructure, resembling a marigold with an open-ended accessible pore structure, is referred to as nanocarbon florets (NCFs, Figure 1a and Figure S1b,c).

The hard-carbon structure of the NCF is confirmed from both vibrational characteristics and the microscopic evaluation. Micro-Raman spectroscopy of the NCF exhibits two main features corresponding to the D-band (1351 cm^{-1}) and G-band (1599 cm^{-1}, Figure 1g). Specifically, while the G-band is associated with the in-plane tangential vibrations, the D-band is originated due to two-photon absorption followed by transition in momentum space from Γ to Γ′ without going through a nonradiative pathway, characteristic of intrinsically disordered systems.[44] Further the absence of any component at 1331 cm^{-1} clearly rules out the possibility of any sp^3 C centers in the NCF. Finally, the second-order peaks are broad and unresolvable, signifying the disordered graphitic domains. This is further confirmed from structural analysis through HR-TEM that reveals the presence of short-range graphitic ordering with an enlarged d-spacing of 0.4 nm along with intrinsic disorder in the long range (Figure S3b and Figure 3i). Consequently, electron diffraction reveals a large amorphous background (Figure S3c). The X-ray diffractogram confirms this understanding with a broad (001) diffraction pattern at 24.9° in agreement with the TEM image (Figure S3a). Thus, the combination of these observations irrefutably confirms the hard-carbon nature of the NCF. Finally, the unique morphology with the open-ended structure provides a highly accessible surface area (~936 m^2/g) and large pore volume that is composed of both micropores (20%) and mesopores (80%), as seen from Figure S3d. Thus, the NCF represents a novel combination of intrinsically disordered structure assembled into a hierarchically dendritic morphology.

https://doi.org/10.1021/acsmaterialsau.1c00062
ACS Mater. Au 2022, 2, 154−162

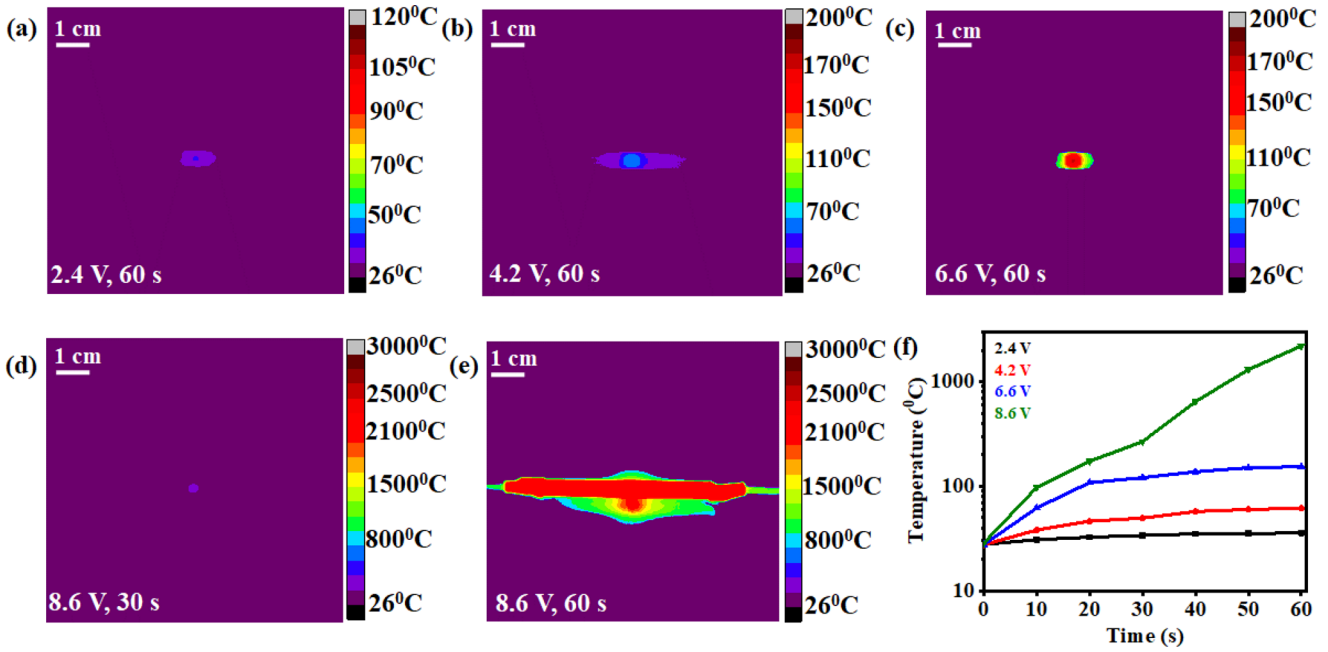

Figure 2. Infrared-based thermometric images of the sample at various V_i values of (a) 2.4 V at 60 s, (b) 4.2 V at 60 s, (c) 6.6 V at 60 s, (d) 8.6 V at 30 s, and (e) 8.6 V at 60 s. (f) Temporal evolution of temperatures at different input voltages.

The NCF presents interesting possibilities for understanding structural transformations among carbon allotropes. As opposed to approaches involving thermal sintering and ion bombardment,[45] we based our design principles on an electric field-driven structural change. The advantage of this approach is the precise control over the transformation, leading to uniformity in the resulting structure (vide infra). Such an approach has not been adopted in earlier investigations, primarily due to (a) the non-availability of porous, nanostructured hard-carbon precursors, (b) high electromigrative resistance of available soft-carbon precursors, and (c) high electrical resistivity of nanodiamonds (2.5×10^8 Ω cm) when compared to NCF (14.2 Ω cm, 0.07 S/cm).

The NCF is packed into a cylindrical column of a quartz capillary at a packing density of 1.27 g/cm^3 to achieve an electrical conductivity of 0.07 S/cm that was maintained constant for all the experiments (Figure 1a,b). An input voltage (V_i) was employed to create an electric field (1.7×10^3 V/m), leading to a current density of 764.3 A/cm^2 (Figure 1e). Although significantly lower than the electromigrative threshold for nanocarbons (~10^6 A/cm^2),[46] the high electrical resistivity of the column ensures the corresponding Joule heating. Thereby, it is proposed that the combination of electromigrative and thermomigrative forces drives the observed structural transformations.

The structural and chemical transformations driven by V_i are evident from the pronounced increase in electrical conductivity from 0.07 S/cm (at V_i = 0 V) to 4.17 S/cm (at V_i = 8.6 V), representing a ~5700% enhancement of electrical conductivity (Figure 1e and Figure S4). This sets up an autocatalytic process where the lowering of resistivity increases the magnitude of current and therefore triggers the transformation in the NCF column. The change in electrical resistivity was monitored by applying a pulse voltage (V_p) that is significantly smaller than V_i and therefore cannot play any role in the changes observed. Finally, the system exhibits an ohmic behavior for the entire range of V_i (Figure 1e and Figure S4).

The first confirmation of the structural transformation originates from the conversion of the packed NCF column into a self-standing cylindrical monolith (1 mm in diameter, 5 mm in length, Figure 1a,b). The free-standing structure is a consequence of thermo-electromigration driving the fusion of adjacent NCFs. It is evident that the packing density and the electrical contacting are insufficient to drive this transformation. Detailed experiments were carried out to understand the pathway of such transformations and the structure of the resulting monolith. Pristine NCF exhibits two characteristic peaks corresponding to the graphitic (002) and (100) reflections, corresponding to a d-spacing of 0.4 nm (Figure 1f and Figure S3a). Although these peaks are retained upon transformation to the monolith, their positions and FWHM undergo distinct changes. The (002) peak exhibits a shift to higher angles, indicative of a reduction in the d-spacing (0.29 nm) for the monolith (Figure 1f). Further, the FWHM of the (002) reflection broadens for the monolith due to the lowering of domain sizes brought about by the interlinking of the NCF. Another marked change is the superimposition of a strong asymmetric graphitic (100) reflection plane over the broad feature present in pristine NCF (Figure 1f). These observations are corroborated by the XPS results that exhibit an invariant C 1s peak at 284.6 eV originating from the sp^2 carbon content (Figure S5a). It is important to note that the O 1s peak shifts to a lower binding energy in the monolith, possibly due to the aerial conditions under which the experiment is carried out (Figure S5b).

Given that both electric fields and associated thermal fields are simultaneously applied on the NCF column, it is important to decouple and understand each role separately. Accordingly, in situ infrared thermometric images reveal that the surface temperature of the NCF column increases to ~2200 °C at a V_i of 8.6 V (Figure 2e and Figure S6a−g). This confirms the thermomigrative field as the primary driver for the observed transformation since the current density (764.3 A/cm^2 at V_i = 8.6 V) is insufficient to drive electromigration in nanocarbons.

https://doi.org/10.1021/acsmaterialsau.1c00062
ACS Mater. Au 2022, 2, 154−162

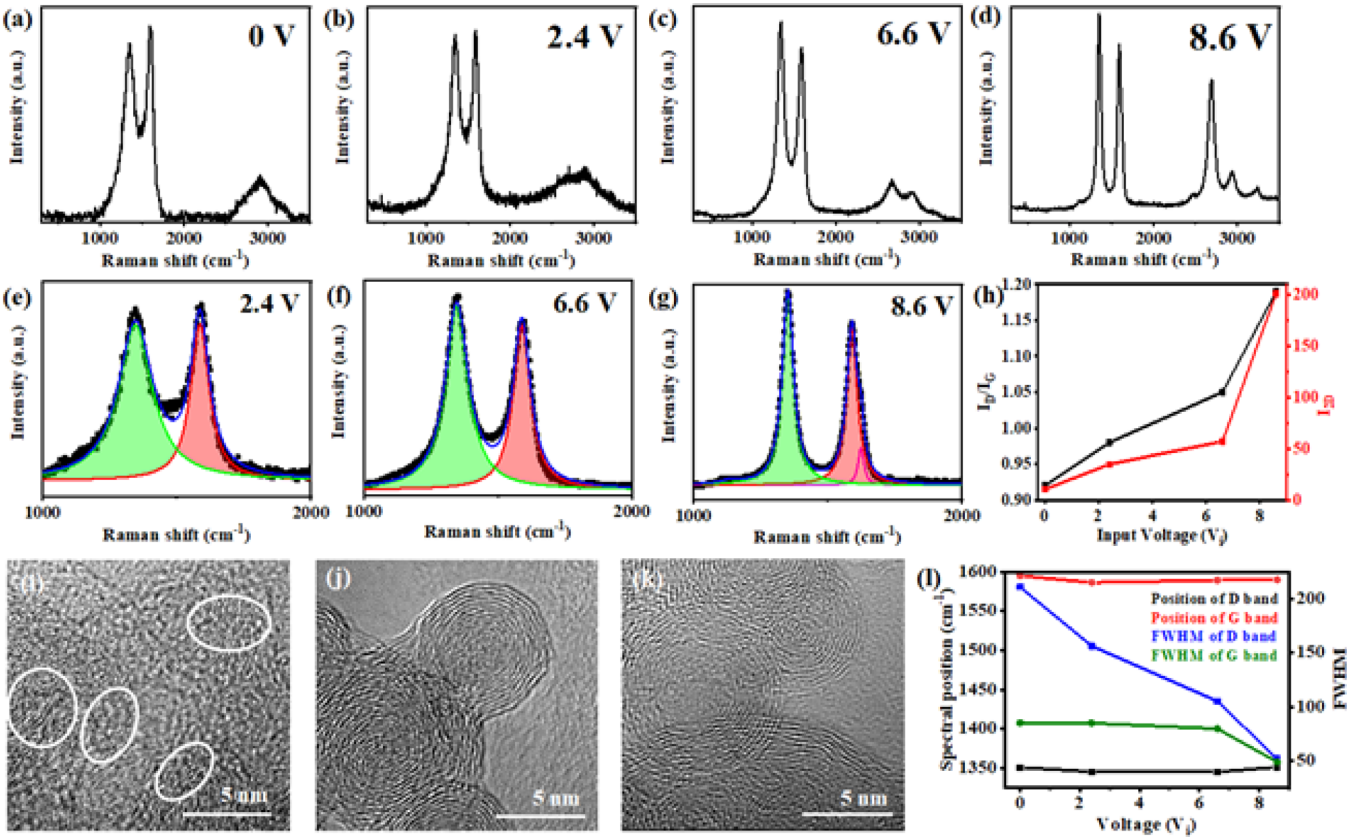

Figure 3. Raman spectra at different input voltages: (a) 0 V, (b) 2.4 V, (c) 6.6 V, and (d) 8.6 V. Deconvoluted Raman spectra of samples subjected to V_i values of (e) 2.4 V, (f) 6.6 V, and (g) 8.6 V. (h) Variation of I_D/I_G ratios and I_{2D} with V_i. HR-TEM of (i) NCFs (white circles showing long-range disordered graphitic domains) and (j) and (k) OLCMs. (l) Variation of spectral positions and FWHM of D- and G-bands at various V_i values.

However, the high resistivity of the NCF column (14.2 Ω cm) and the current flow (6 A at V_i = 8.6 V) are critical for resistive Joule heating that drives the transformation of the NCF to the monolith (Figure S4). Furthermore, an increase in V_i results in both the higher temperature of the hotspot and longer time to reach the steady-state temperature. (Figure 2f and Figures S7–S9). V_i is the driving force for the Joule heating, and therefore larger V_i results in a higher temperature in the NCF column. Alongside the voltage-induced Joule heating, the thermal dissipation of the NCF column dictates the higher temperature of the hotspot and the longer time taken for reaching the steady-state temperature. These observations are coupled to the structural transformation of NCFs to OLCMs. Thus, the use of current becomes a versatile handle to control the dynamics and uniformity of such transformations in hard-carbon nanostructures.

The evolution of temperature during the process is an indication of the kinetics of the transformation of the NCF into a free-standing monolith. It is observed that the magnitude of steady-state temperature and the time taken to reach the steady state are both monotonically proportional to the magnitude of V_i (Figure 2f). Thus, the rate of temperate increase is 0.15 °C/s for a V_i of 2.4 V, leading to saturation at ∼36 °C within 30 s (Figures S6–S9). In contrast, a larger V_i (8.6 V) results in a steeper increase in temperature (36.2 °C/s) and a delayed onset of the steady-state temperature (2200 °C at 60 s), again underlining the thermal contribution to the transformation observed (Figure 2f).

In-depth structural analysis of the free-standing NCF monolith is carried out through micro-Raman spectroscopy and HR-TEM. As discussed above, the Raman spectrum of the pristine NCF confirms its hard-carbon nature and disordered domain orientation. No deviation of this is observed after packing the NCF into the quartz capillary (Figure 3a). Application of V_i is accompanied by distinct changes in the spectral features. The first noticeable feature is the inversion of the intensities of D- and G-bands upon increasing the V_i from 0 to 2.4 V (Figure 3b,e). Although prominent, the intensity of the D-band (I_D at 1341 cm^{-1}) is lower than the G-band (I_G at 1585 cm^{-1}) in the NCF (Figure 3a). The I_D/I_G ratio changes from 0.92 to 0.98 at a V_i of 2.4 V and further increases to 1.0 at a V_i of 6.6 V, reaching 1.2 at a V_i of 8.6 V (Figure 3h). Such a monotonic increase in I_D/I_G at a higher V_i is in complete contrast to earlier observations,[47,48] where lowering of the I_D/I_G ratio is conventionally observed and attributed to an increase in graphitic crystallization.

Concomitantly, the D-band shows significant stiffening with an increase in V_i (Figure 3e–g,l). The sharpening of the D-band is also accompanied by the emergence of two distinct peaks at 2712 and 2936 cm^{-1} corresponding to 2D and G + D modes (Figure 3d). The sharp signature at 2712 cm^{-1} in the OLCM is close to the value of HOPG (2719 cm^{-1})[49] and originates from the graphitic ordering of the nested onion-like carbon shells in the monolith (OLCMs). Both the D + D′ mode (originating from the double resonance process) and the G′ mode are confirmative of the few layer disordered graphene that makes up the structure of the NCF. The conversion of the

https://doi.org/10.1021/acsmaterialsau.1c00062
ACS Mater. Au 2022, 2, 154–162

NCF to OLCM is accompanied by the lowering of the structural disorder due to which this peak disappears and is replaced with sharp peaks attributed to the 2D and D + G modes (Figure 1g and Figure 3h,l). Further, there is no component corresponding to sp^3 C centers as seen from the complete absence of any component at 1331 cm^{-1} (Figure 3e−g). Importantly, the increase in the I_D/I_G ratio is concurrent with the increase in the intensity of the 2D-band (I_{2D}, Figure 3h). The intense and sharp 2D-band is indicative of the defect-free nature of the graphitic domains that form the OLCs. Such an increase in ordering from the hard-carbon NCF is triggered by temperature. Such temperature-induced defect healing drives the transformation toward the thermodynamically stable spherical assembly.[48] However, an important difference in this work is the hard-carbon origin of the OLCMs, rather than from diamonds or soft-carbons.

Thus, the transformation of NCFs to OLCMs is proposed to proceed from the surface to the core of the OLCs and therefore precludes the formation of a nanodiamond core. Further, the NCF with its intrinsic disordered domain structure is not converted to graphitic crystals but rather transforms into a spherically nested onion-like carbon structure. Such a transformation is completed at 8.6 V, as seen from the perfectly separated and resolved second-order peaks (Figure 3d). These observations conclusively pinpoint the monolith to be composed of onion-like carbons, and therefore, it is henceforth referred to as onion-like carbon monoliths (OLCMs). It is important to note that the final values of FWHM of the D- and G-bands for OLCMs are in excellent agreement with those reported earlier (Figure 3l and Figure S10a−e).[48,49] Furthermore, the spectral positions of the D- and G-bands remain invariant throughout the transformations. This again presents a contrasting observation compared to the OLCs obtained from nanodiamonds. Herein, the nanodiamonds carry a strong sp^3 character and therefore have to necessarily go through an sp^3−sp^2 structural transformation to reach graphitic ordering. In contrast, the hard-carbon NCF in our case is already composed of graphitic domains that are randomly oriented with respect to each other. Thus, the thermo-electrical driving force is responsible for the reorganization of these domains, leading to a proportionate increase in the intensity of D-band, 2D-band, and D + G modes (Figure 1g and Figure 3l).

The observations from micro-Raman are conclusively supported from the HR-TEM images of the OLCMs, which show clear nested spheres with excellent ordering and stacking (Figure 3j,k and Figure S11). The average size of the OLCs is 6.5 ± 1.2 nm, made up of ∼12−14 layers (Figure S11). This supports the strong and sharp phonon modes seen in the Raman spectra of samples after a V_i of 8.6 V and is supported by a semi-emperical Tersoff model.[50] Further, a nondiamond core is observed, supporting the absence of the diamond line in OLCMs. The fusion of the outer graphitic shells with each other, leading to the formation of a monolithic structure, is also observed in the TEM images.

Further validation of these arguments demands that these spectral features be uniformly observed across macroscopic dimensions of the sample. Accordingly, diffraction-limited micro-Raman spectral maps were carried out based on the intensities and FWHMs of the D, G, and 2D modes. Complete retention of all spectroscopic signatures corresponding to OLCs was observed throughout the macroscopic area (10^4 μm^2) consisting of 10,000 spectral points (Figure 4a,c,d).

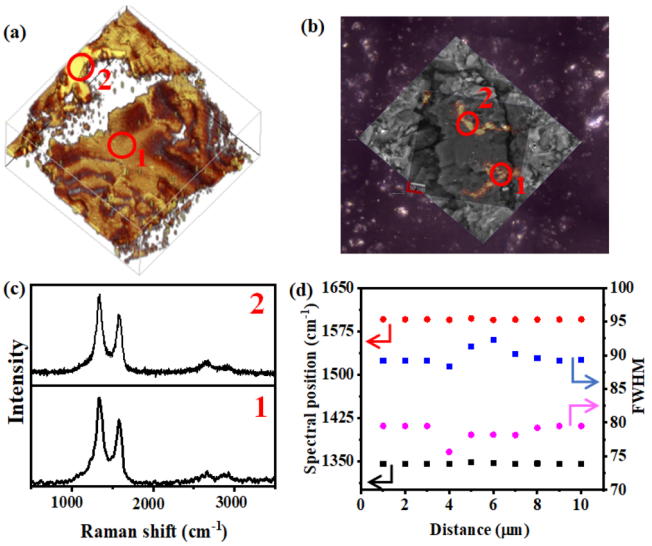

Figure 4. (a) 3D Raman volume map based on the intensity of D-bands. (b) Correlative SEM imaging superimposed on the Raman map profile. (c) Raman spectra corresponding to the labeled regions on (a) and (b). (d) Spectral positions and FWHM of D- and G-bands estimated from the line profile spectra that are recorded over a distance of 10 μm on the cross section of OLCMs.

Further confirmation of uniformity is also the fact that the spectral features were invariant across the multiple areas acquired on both the surface and cross section of OLCMs (Figure 4c). Confocal slices of OLCMs were used to reconstruct the three-dimensional morphology that was also in excellent agreement with the two-dimensional spectral maps (Figure 4a and Figure S12). In addition, such three-dimensional spectral reconstruction enabled correlation with the morphological information in SEM images (Figure 4b). Finally, the structural evolution of the NCF to OLCM and the accompanying morphological changes (Figures S13 and S14) are consistent with the spectroscopic conclusions.

The ambient conditions under which the transformations occur provide a distinct possibility of the chemical functionalization of the OLCMs. The X-ray photoelectron spectra of the OLCMs exhibit a well-defined, characteristic C 1s peak at 284.6 eV corresponding to the C═C network (Figure S5a). The C 1s also reveals an additional component at 288.8 eV corresponding to C═O functionality, which is also confirmed from the O 1s peaks (Figure S5b). Such partial and controlled oxidation of the OLCMs is further confirmed from the fluorescence lifetime measurements (Figure 5a−d). Excited-state lifetime studies on the solid-state OLCMs (λ_{ex} at 532 nm) reveal a biexponential nanosecond decay, in agreement with earlier reports (Table T2).[51] Importantly, the τ_1 lifetime component at 3.4 ns dominated the entire area of the sample with a single-modal, sharp peak in the histogram, confirming the uniformity of the sample (Figure 5d and Table T2).

The free-standing porous nature of the OLCMs points to several interesting applications in the domains of energy storage[28,29] and environmental remediation.[51−53] In this direction, the extensive graphitic surface of the OLCMs was exploited to adsorb and trap VOCs such as toluene. The experiments were conducted with toluene as the model VOC in flow-through geometry to mimic the smoke filter of a cigarette. Further, the concentration range (0.22−1.86 ppm), ambience (N_2, O_2, and toluene), and flow rates (100 sccm)

https://doi.org/10.1021/acsmaterialsau.1c00062
ACS Mater. Au 2022, 2, 154−162

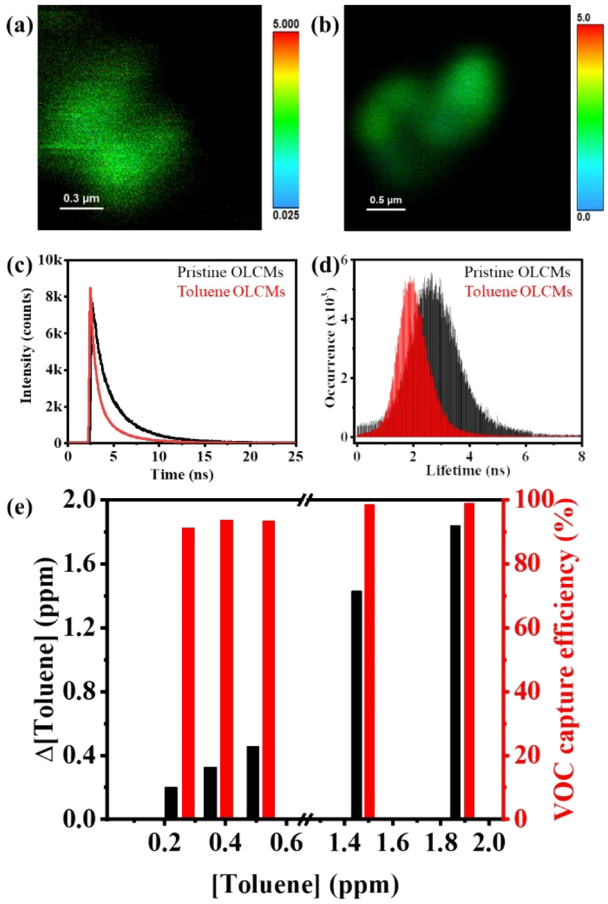

Figure 5. Color-coded image of 2.25 μm^2 area of OLCMs based on the fluorescence lifetimes, recorded (a) before and (b) after exposure to toluene. The color scale bars represent the average lifetime in nanoseconds. (c) Fluorescence lifetime decay measured on pristine OLCMs (black) and those exposed to toluene (red). (d) Histogram of the fluorescence lifetime distribution across the entire area. (c) Change in the concentration of toluene and the VOC capture efficiencies of OLCMs over a concentration range of toluene (0.22–1.86 ppm).

studied are of direct significance and relevance to the conditions encountered during smoking of cigarettes (0.26 ppm).[54]

A significant decrease in the concentration of VOC (toluene) was observed across the entire spectrum, signifying an effective uptake by OLCMs (Figure 5e). The absolute decrease in the concentration of toluene vapors is proportional to the initial concentration of toluene. Accordingly, the VOC capture efficiency was estimated as

$$\text{VOC capture efficiency} = ([C]_{in} - [C]_f)/[C]_{in} \times 100$$

where $[C]_{in}$ is the initial concentration of toluene and $[C]_f$ is the final concentration of toluene. It is observed that the VOC capture efficiency is uniformly high across all $[C]_{in}$ investigated (Figure 5c). This indicates that the diffusion of VOCs through the pores of OLCMs drives their capture. Herein, the graphitic surface of OLC facilitates the trapping of toluene through $\pi-\pi$ interactions while the porosity of OLCM ensures minimal pressure drop across it.

Further experiments are carried out to comprehend the mechanism of capture of toluene by OLCMs. Herein, the D-band and G-band in the used OLCMs (after exposure to toluene) exhibit peak broadening along with a shift to lower wavenumbers compared to pristine OLCMs (Figure S15 and Table T1). This is attributed to the tensile stress developed in the OLCMs due to the incorporation of toluene within the OLCMs. This is also reflected in the lowering of fluorescence lifetime of the used OLCMs when compared to pristine OLCMs (Figure 5 and Table T2). Further, the lowering of the radiative decay lifetime also indicates the $\pi-\pi$-based interaction between toluene and the OLCMs. These results also expand the scope of the applicability of OLCMs for both detection and capture of volatile organic compounds such as toluene. Finally, the OLCMs show structural integrity and retain the structure after exposure to toluene, as seen from the TEM images (Figure S16), confirming their stability.

The capture of toluene is also reflected in the increase in the resistance of the OLCM from 3.4 Ω for pristine to 42.1 Ω after capture of toluene (Figure S17). This also points to the possibility that toluene is captured both on the surface and within the layers of the OLCM. The excellent VOC capture efficiency is consistently above 90% over the entire range of concentrations tested. The thermal stability of the OLCM and its high VOC capture efficiency points to its direct applicability in VOC filters.

CONCLUSIONS

In summary, besides providing concrete design principles for fabrication of porous nanostructure hard-carbons, their structural transformation driven by thermal and electric fields leading to the formation of monolithic porous onion-like carbon macrostructures is demonstrated. The fundamental pathway leading to the reorganization of the randomly oriented graphitic domains to form curved and nested carbon onions is elucidated through a combination of in situ thermometry and ex situ spectroscopic and microscopic techniques. These point to the importance of Joule heating in leading the transformation. The precise and tunable approach presented is distinctly different from other sp^3 to sp^2 pathways and results in monolithic structures that are hitherto not observed. Such OLCMs have excellent VOC capture efficiency and thermal stability and thereby provides transformative opportunities in domains of energy storage, heterogeneous catalysis, and similar interfacial applications.

ASSOCIATED CONTENT

Supporting Information

The Supporting Information is available free of charge at https://pubs.acs.org/doi/10.1021/acsmaterialsau.1c00062.

SEM, pXRD, HR-TEM, and BET curves of DFNS and NCFs; SEM images, HR-TEM image, and line profile of the OLCM; resistivity trend of the NCF to OLCM when subjected to 0–8.6 V; C 1s and O 1s XPS spectra of the NCF vs OLCM; IR thermal images of the OLCM at different time intervals when subjected to 2.4, 4.2, 6.6, and 8.6 V; IR thermal image of the packed NCF inside a quartz tube at 0 V and temperature vs time profile of the OLCM showing saturation at 2200 °C for 8.6 V at 120 s; deconvoluted Raman spectra to show uniformity in D- and G-bands across a 10 μm scale of the OLCM; 3D Raman maps containing confocal slices of the OLCM of G- and 2D-bands; SEM images showing the morphology of the NCF at various scales in comparison to SEM images showing morphology of the OLCM at various

https://doi.org/10.1021/acsmaterialsau.1c00062
ACS Mater. Au 2022, 2, 154–162

scales; *IV* characteristic of the OLCM after VOC (toluene) capture; and fluorescence lifetime measurements of the OLCM (PDF)

AUTHOR INFORMATION

Corresponding Author

Chandramouli Subramaniam − *Department of Chemistry, Indian Institute of Technology Bombay, Mumbai 400076 Maharashtra, India;* orcid.org/0000-0001-8335-7395; Email: csubbu@chem.iitb.ac.in

Author

Itisha Dwivedi − *Department of Chemistry, Indian Institute of Technology Bombay, Mumbai 400076 Maharashtra, India*

Complete contact information is available at: https://pubs.acs.org/10.1021/acsmaterialsau.1c00062

Author Contributions

I.D. and C.S. conceptualized the experiments, interpreted the data, and co-wrote the manuscript. I.D. conducted the experiments.

Notes

The authors declare no competing financial interest.

ACKNOWLEDGMENTS

We thank SERB, New Delhi and Department of Science and Technology, Government of India for financial support (grants SERB/F/9022/2019−2020 and DST-SwarnaJayanti Fellowship to C.S.). I.D. acknowledges the support provided by the University Grants Commission (UGC), India to pursue research work.

ABBREVIATIONS

OLCM	onion-like carbon monolith
DFNS	dendritic fibrous nanosilica
NCF	nanocarbon floret
VOCs	volatile organic compounds

REFERENCES

(1) Castro, E.; Garcia, A. H.; Zavala, G.; Echegoyen, L. Fullerenes in Biology and Medicine. *J. Mater. Chem. B* **2017**, *5*, 6523−6535.

(2) Futaba, D. N.; Hata, K.; Yamada, T.; Hiraoka, T.; Hayamizu, Y.; Kakudate, Y.; Tanaike, O.; Hatori, H.; Yumura, M.; Iijima, S. Shape-Engineerable and Highly Densely Packed Single-Walled Carbon Nanotubes and Their Application as Super-Capacitor Electrodes. *Nat. Mater.* **2006**, *5*, 987−994.

(3) Yamada, T.; Hayamizu, Y.; Yamamoto, Y.; Yomogida, Y.; Izadi-Najafabadi, A.; Futaba, D. N.; Hata, K. A Stretchable Carbon Nanotube Strain Sensor for Human-Motion Detection. *Nat. Nanotechnol.* **2011**, *6*, 296−301.

(4) Taychatanapat, T.; Bolotin, K. I.; Kuemmeth, F.; Ralph, D. C. Imaging Electromigration during the Formation of Break Junctions. *Nano Lett.* **2007**, *7*, 652−656.

(5) Zettl, A. Extreme Oxygen Sensitivity of Electronic Properties of Carbon Nanotubes. *Science* **2000**, *287*, 1801−1804.

(6) Joo, S. H.; Park, J. Y.; Tsung, C. K.; Yamada, Y.; Yang, P.; Somorjai, G. A. Thermally Stable Pt/Mesoporous Silica Core-Shell Nanocatalysts for High-Temperature Reactions. *Nat. Mater.* **2009**, *8*, 126−131.

(7) Kim, H.; Jin, C.; Park, S.; Kim, S.; Lee, C. H 2S Gas Sensing Properties of Bare and Pd-Functionalized CuO Nanorods. *Sens. Actuators, B* **2012**, *161*, 594−599.

(8) Maye, M. M.; Lou, Y.; Zhong, C. J. Core-Shell Gold Nanoparticle Assembly as Novel Electrocatalyst of CO Oxidation. *Langmuir* **2000**, *16*, 7520−7523.

(9) Li, X.; Li, T.; Ma, Y.; Wei, Q.; Qiu, W.; Guo, H.; Shi, X.; Zhang, P.; Asiri, A. M.; Chen, L.; Tang, B.; Sun, X. Boosted Electrocatalytic N2 Reduction to NH3 by Defect-Rich MoS2 Nanoflower. *Adv. Energy Mater.* **2018**, *8*, 1−8.

(10) Subramaniam, C.; Yamada, T.; Kobashi, K.; Sekiguchi, A.; Futaba, D. N.; Yumura, M.; Hata, K. One Hundred Fold Increase in Current Carrying Capacity in a Carbon Nanotube-Copper Composite. *Nat. Commun.* **2013**, *4*, 1−7.

(11) Pesetski, A. A.; Baumgardner, J. E.; Folk, E.; Przybysz, J. X.; Adam, J. D.; Zhang, H. Carbon Nanotube Field-Effect Transistor Operation at Microwave Frequencies. *Appl. Phys. Lett.* **2006**, *88*, 1−4.

(12) Ho, P. S.; Kwok, T. Electromigration in Metals. *Reports Prog. Phys.* **1989**, *52*, 301−348.

(13) Shaik, S.; Ramanan, R.; Danovich, D.; Mandal, D. Structure and Reactivity/Selectivity Control by Oriented-External Electric Fields. *Chem. Soc. Rev.* **2018**, *47*, 5125−5145.

(14) Wang, C.; Danovich, D.; Chen, H.; Shaik, S. Oriented External Electric Fields: Tweezers and Catalysts for Reactivity in Halogen-Bond Complexes. *J. Am. Chem. Soc.* **2019**, *141*, 7122.

(15) Wilhite, P.; Vyas, A. A.; Tan, J.; Tan, J.; Yamada, T.; Wang, P.; Park, J.; Yang, C. Y. Metal-Nanocarbon Contacts. *Semicond. Sci. Technol.* **2014**, *29*, 054006.

(16) Subramaniam, C.; Sreeprasad, T. S.; Pradeep, T.; Pavan Kumar, G. V.; Narayana, C.; Yajima, T.; Sugawara, Y.; Tanaka, H.; Ogawa, T.; Chakrabarti, J. Visible Fluorescence Induced by the Metal Semiconductor Transition in Composites of Carbon Nanotubes with Noble Metal Nanoparticles. *Phys. Rev. Lett.* **2007**, *99*, 1−4.

(17) Ajayan, P. M.; Terrones, M.; De la Guardia, A.; Huc, V.; Grobert, N.; Wei, B. Q.; Lezec, H.; Ramanath, G.; Ebbesen, T. W. Nanotubes in a Flash - Ignition and Reconstruction. *Science* **2002**, *296*, 705.

(18) Ruan, G.; Sun, Z.; Peng, Z.; Tour, J. M. Growth of Graphene from Food, Insects, and Waste. *ACS Nano* **2011**, *5*, 7601−7607.

(19) Luong, D. X.; Bets, K. V.; Algozeeb, W. A.; Stanford, M. G.; Kittrell, C.; Chen, W.; Salvatierra, R. V.; Ren, M.; McHugh, E. A.; Advincula, P. A.; Wang, Z.; Bhatt, M.; Guo, H.; Mancevski, V.; Shahsavari, R.; Yakobson, B. I.; Tour, J. M. Gram-Scale Bottom-up Flash Graphene Synthesis. *Nature* **2020**, *577*, 647−651.

(20) Cammidge, A. N.; Crepy, K. V. L. The First Asymmetric Suzuki Cross-Coupling Reaction. *Chem. Commun.* **2000**, *18*, 1723−1724.

(21) Dutta, U.; Maiti, S.; Bhattacharya, T.; Maiti, D. Arene Diversification through Distal C(Sp2)-H Functionalization. *Science* **2021**, *372*, eabd5992.

(22) Cao, Y.; Fatemi, V.; Fang, S.; Watanabe, K.; Taniguchi, T.; Kaxiras, E.; Jarillo-Herrero, P. Unconventional Superconductivity in Magic-Angle Graphene Superlattices. *Nature* **2018**, *556*, 43−50.

(23) Gogotsi, Y. *Science* **2010**, *330*, 1332.

(24) Kuznetsov, V. L.; Chuvilin, A. L.; Butenko, Y. V.; Yu, I.; Titov, V. M. Onion-like Carbon from Ultra-Disperse Diamond. *Chem. Phys. Lett.* **1994**, *222*, 343−348.

(25) Rettenbacher, A. S.; Elliott, B.; Hudson, J. S.; Amirkhanian, A.; Echegoyen, L. Preparation and Functionalization of Multilayer Fullerenes (Carbon Nano-Onions). *Chem. - A Eur. J.* **2005**, *12*, 376−387.

(26) Palkar, A.; Melin, F.; Cardona, C. M.; Elliott, B.; Naskar, A. K.; Edie, D. D.; Kumbhar, A.; Echegoyen, L. Reactivity Differences between Carbon Nano Onions (CNOs) Prepared by Different Methods. *Chem. - An Asian J.* **2007**, *2*, 625−633.

(27) Leyssale, J. M.; Vignoles, G. L. Molecular Dynamics Evidences of the Full Graphitization of a Nanodiamond Annealed at 1500 K. *Chem. Phys. Lett.* **2008**, *454*, 299−304.

(28) Pech, D.; Brunet, M.; Durou, H.; Huang, P.; Mochalin, V.; Gogotsi, Y.; Taberna, P. L.; Simon, P. Ultrahigh-Power Micrometre-Sized Supercapacitors Based on Onion-like Carbon. *Nat. Nanotechnol.* **2010**, *5*, 651−654.

(29) Borgohain, R.; Li, J.; Selegue, J. P.; Cheng, Y. T. Electrochemical Study of Functionalized Carbon Nano-Onions for High-Performance Supercapacitor Electrodes. *J. Phys. Chem. C* **2012**, *116*, 15068−15075.
(30) Hirata, A.; Igarashi, M.; Kaito, T. Study on Solid Lubricant Properties of Carbon Onions Produced by Heat Treatment of Diamond Clusters or Particles. *Tribol. Int.* **2004**, *37*, 899−905.
(31) Sano, N.; Wang, H.; Alexandrou, I.; Chhowalla, M.; Teo, K. B. K.; Amaratunga, G. A. J.; Iimura, K. Properties of Carbon Onions Produced by an Arc Discharge in Water. *J. Appl. Phys.* **2002**, *92*, 2783−2788.
(32) Kroto, H.; Heath, J.; O'Brien, S.; Curl, R. F.; Smalley, R. E. C_{60}: Buckminsterfullerene. *Nature* **1985**, *318*, 162−163.
(33) Pop, E.; Mann, D.; Wang, Q.; Goodson, K.; Dai, H. Thermal Conductance of an Individual Single-Wall Carbon Nanotube above Room Temperature. *Nano Lett.* **2006**, *6*, 96−100.
(34) *Proc. Anal. Div. Chem. Soc.* **1977**, *14* (2), 44−46, .
(35) Wang, Q.; Zhu, X.; Liu, Y.; Fang, Y.; Zhou, X.; Bao, J. Rice Husk-Derived Hard Carbons as High-Performance Anode Materials for Sodium-Ion Batteries. *Carbon N. Y.* **2018**, *127*, 658−666.
(36) He, Y.; Xu, Y.; Li, J.; Xu, Z.; Zhang, Z.; Sun, J.; Zhang, M.; Zhu, X.; Zhou, X. Core-Shell Structured Fe7S8@C Nanospheres as a High-Performance Anode Material for Potassium-Ion Batteries. *Energy Fuels* **2021**, *35*, 3490−3496.
(37) Saha, J.; Ball, R.; Sah, A.; Kalyani, V.; Subramaniam, C. The Mechanistic Role of a Support-Catalyst Interface in Electrocatalytic Water Reduction by Co3O4 Supported Nanocarbon Florets. *Nanoscale* **2019**, *11*, 13532−13540.
(38) Wang, Q.; Ge, X.; Xu, J.; Du, Y.; Zhao, X.; Si, L.; Zhou, X. Fabrication of Microporous Sulfur-Doped Carbon Microtubes for High-Performance Sodium-Ion Batteries. *ACS Appl. Energy Mater.* **2018**, *1*, 6638−6645.
(39) Saha, J.; Verma, S.; Ball, R.; Subramaniam, C.; Murugavel, R. Compositional Control as the Key for Achieving Highly Efficient OER Electrocatalysis with Cobalt Phosphates Decorated Nanocarbon Florets. *Small* **2020**, *16*, 1903334.
(40) Jha, M. K.; Babu, B.; Parker, B. J.; Surendran, V.; Cameron, N. R.; Shaijumon, M. M.; Subramaniam, C. Hierarchically Engineered Nanocarbon Florets as Bifunctional Electrode Materials for Adsorptive and Intercalative Energy Storage. *ACS Appl. Mater. Interfaces* **2020**, *12*, 42669−42677.
(41) Maity, A.; Das, A.; Sen, D.; Mazumder, S.; Polshettiwar, V. Unraveling the Formation Mechanism of Dendritic Fibrous Nanosilica. *Langmuir* **2017**, *33*, 13774−13782.
(42) Mishra, A. K.; Belgamwar, R.; Jana, R.; Datta, A.; Polshettiwar, V. Defects in Nanosilica Catalytically Convert CO2 to Methane without Any Metal and Ligand. *Proc. Natl. Acad. Sci. U. S. A.* **2020**, *117*, 6383−6390.
(43) Iveković, A.; Dražić, G.; Novak, S. Densification of a SiC-Matrix by Electrophoretic Deposition and Polymer Infiltration and Pyrolysis Process. *J. Eur. Ceram. Soc.* **2011**, *31*, 833−840.
(44) Euchner, H.; Vinayan, B. P.; Reddy, M. A.; Fichtner, M.; Groß, A. Alkali Metal Insertion into Hard Carbon-the Full Picture. *J. Mater. Chem. A* **2020**, *8*, 14205−14213.
(45) McDonough, J. K.; Gogotsi, Y. Carbon Onions: Synthesis and Electrochemical Applications. *Electrochem. Soc. Interface* **2013**, *22*, 61−66.
(46) Subramaniam, C.; Sekiguchi, A.; Yamada, T.; Futaba, D. N.; Hata, K. Nano-Scale, Planar and Multi-Tiered Current Pathways from a Carbon Nanotube-Copper Composite with High Conductivity, Ampacity and Stability. *Nanoscale* **2016**, *8*, 3888−3894.
(47) Korepanov, V. I.; Hamaguchi, H. o.; Osawa, E.; Ermolenkov, V.; Lednev, I. K.; Etzold, B. J. M.; Levinson, O.; Zousman, B.; Epperla, C. P.; Chang, H. C. Carbon Structure in Nanodiamonds Elucidated from Raman Spectroscopy. *Carbon N. Y.* **2017**, *121*, 322−329.
(48) Cebik, J.; McDonough, J. K.; Peerally, F.; Medrano, R.; Neitzel, I.; Gogotsi, Y.; Osswald, S. Raman Spectroscopy Study of the Nanodiamond-to-Carbon Onion Transformation. *Nanotechnology* **2013**, *24*, 205703.
(49) Roy, D.; Chhowalla, M.; Wang, H.; Sano, N.; Alexandrou, I.; Clyne, T. W.; Amaratunga, G. A. J. Characterisation of Carbon Nano-Onions Using Raman Spectroscopy. *Chem. Phys. Lett.* **2003**, *373*, 52−56.
(50) Tersoff, J. Empirical Interatomic Potential for Carbon, with Applications to Amorphous Carbon. *Phys. Rev. Lett.* **1988**, *61*, 2879−2882.
(51) Tripathi, K. M.; Tran, T. S.; Kim, Y. J.; Kim, T. Y. Green Fluorescent Onion-Like Carbon Nanoparticles from Flaxseed Oil for Visible Light Induced Photocatalytic Applications and Label-Free Detection of Al(III) Ions. *ACS Sustainable Chem. Eng.* **2017**, *5*, 3982−3992.
(52) Moronshing, M.; Sah, A.; Kalyani, V.; Subramaniam, C. Nanostructured Carbon Florets as Scavenger of As3+, Cr6+, Cd2+, and Hg2+ for Water Remediation. *ACS Appl. Nano Mater.* **2020**, *3*, 468−478.
(53) Mondal, S.; Subramaniam, C. Scalable Approach towards Specific and Ultrasensitive Cation Sensing under Harsh Environmental Conditions by Engineering the Analyte-Transducer Interface. *Nanoscale Adv.* **2021**, *3*, 3752−3761.
(54) Byrd, G. D.; Fowler, K. W.; Hicks, R. D.; Lovette, M. E.; Borgerding, M. F. Isotope Dilution Gas Chromatography-Mass Spectrometry in the Determination of Benzene, Toluene, Styrene and Acrylonitrile in Mainstream Cigarette Smoke. *J. Chromatogr. A* **1990**, *503*, 359−368.

https://doi.org/10.1021/acsmaterialsau.1c00062
ACS Mater. Au 2022, 2, 154−162